crystals

MDPI

Article

Self-Localized Liquid Crystal Micro-Droplet Arrays on Chemically Patterned Surfaces

Jakub Kołacz [1,2,*] and Qi-Huo Wei [1,3,*]

[1] Advanced Materials and Liquid Crystal Institute, Kent State University, Kent, OH 44240, USA
[2] Center for Bio/Molecular Science and Engineering, US Naval Research Lab, Washington, DC 20375, USA
[3] Department of Mechanical and Energy Engineering, Southern University of Science and Technology, Nanshan District, Shenzhen 518055, China
* Correspondence: jakub.kolacz@nrl.navy.mil (J.K.); weiqh@sustech.edu.cn (Q.-H.W.)

Abstract: Liquid crystal (LC) micro-droplet arrays are elegant systems that have a range of applications, such as chemical and biological sensing, due to a sensitivity to changes in surface properties and strong optical activity. In this work, we utilize self-assembled monolayers (SAMs) to chemically micro-pattern surfaces with preferred regions for LC occupation. Exploiting discontinuous dewetting, dragging a drop of fluid over the patterned surfaces demonstrates a novel, high-yield method of confining LC in chemically defined regions. The broad applicability of this method is demonstrated by varying the size and LC phase of the droplets. Although the optical textures of the droplets are dictated by topological constraints, the additional SAM interface is shown to lock in inhomogeneous alignment. The surface effects are highly dependent on size, where larger droplets exhibit asymmetric director configurations in nematic droplets and highly knotted structures in cholesteric droplets.

Keywords: liquid crystal; droplet; microdroplet; microdroplet array; self-assembled monolayers; μ-contact printing; chemical pinning

Citation: Kołacz, J.; Wei, Q.-H. Self-Localized Liquid Crystal Micro-Droplet Arrays on Chemically Patterned Surfaces. *Crystals* **2022**, *12*, 13. https://doi.org/10.3390/cryst12010013

Academic Editors: Chenhui Peng, Dmitry A. Bedrov and Shuang Zhou

Received: 1 November 2021
Accepted: 19 December 2021
Published: 22 December 2021

1. Introduction

Due to their optical activity, LCs in confined geometries are important to a variety of current technologies. In polymer-dispersed LCs, micron-sized LC droplets are directed to either scatter or transmit light by altering the molecular orientation using an external electric field [1], a switching mechanism which has been utilized in smart windows [2]. Microencapsulated cholesteric LCs have a long history as thermochromic paint used for surface thermography in structural materials, microelectronics, fluid mechanics, and medicine [3]. More recently, cholesteric droplets have been exploited to create photonic arrays [4].

LCs also provide a platform for chemical and biological sensing [5,6]. Due to long-range orientational order, the absorption of a small quantity of molecules on LC interfaces can change the surface-anchoring conditions of the LC molecules and lead to changes in the optical properties at the macro-scale. Microfluidic devices that utilize LCs [7,8] are becoming popular because they can be easily incorporated into sensor networks or lab-on-a-chip systems, which are highly desirable for environmental science, forensics, biological warfare, and point-of-care diagnostics. Such devices need high sensitivity to target molecules, fast response to change, portable size, and must be economically and environmentally friendly.

The sensitivity of LCs to surface properties is dependent on LC material properties, surface anchoring, and geometric confinement [9]. The latter is a continuously-tunable variable that changes the LC sensitivity by controlling the ratio of exposed surface area to volume effects of the LC. In free-floating spherical droplets, the ratio is $1/(3r)$, where r is the radius of the droplet. When immobilized as a spherical cap on a surface, the ratio is a more complex function that depends on the contact angle of the droplet. Furthermore, the asymmetry of surfaces, i.e., substrate–liquid vs. liquid–vapor, provides another layer

of complexity. The interplay between long-range interaction length of the LCs and the confinement surface effects creates a rich tapestry of defect structures and transitions.

There are several methods for generating fluid arrays; the most common for LC microarrays use inkjet printing [4,8]. Another attractive option is to use chemically patterned surfaces to exploit chemical pinning [10,11] of a fluid sliding on a surface that results in discontinuous dewetting [12] of a fluid moving over the surface, leaving self-localized microdroplets on the surface [13–15]. In monophilic systems, hydrophilic regions are patterned on hydrophobic or syperhydrophobic surfaces, and the fluid can either be applied by rolling drops across the surface or via dipcoating [16]. This method has been used with aqueous fluids for a wide variety of biological applications [17], with polymers to generate channel waveguides [18] and multiphasic particles [19] and, drawing inspiration from fog-basking Namib desert beetles such as *Stenocara gracilipes*, *Onymacris unguicularis* and *Physosterna cribripes* [20,21], for water harvesting [22], fog-free mirrors, and cancer research [23]. However, chemical patterning to localize LC has only recently been shown in literature [24]. Thermotropic LCs tend to be amphiphilic, making it difficult to find surfaces that are chemically LC-phobic (a contact angle $\theta_c > 90^\circ$).

In this work, we explored the ability of LC to self-localize via chemical pinning [10] on μ-contact printed surfaces [25] using two LC-philic ($\theta_c < 90^\circ$) inks by maximizing the disparity between static contact angles. We note that the wettability of the surface is tied to the molecular orientation on the surface, with planar alignment generally being more favorable than homeotropic alignment. In nematic LCs, we observe optical structures that reflect formation dynamics, surface inhomogeneities, and inherent topological constraints. Cholesteric systems exhibit unique knotting properties that are tied to the size of the chiral pitch inside the drops, able to transform from an ordered spiral to a highly knotted optical texture.

2. Materials and Methods

For contact angle measurement, Au-coated glass was immersed in 1 mM ethanolic solutions of thiol-terminated molecules for one hour for self-assembly, and then a drop of the LC 5CB was placed on the surface using a syringe and imaged using a custom setup.

Chemically patterned surface were fabricated using μ-contact printing (μCP) [25]. To make master molds, negative resist SU8 was spin-coated onto a Si wafer and patterned using contact lithography with a custom photomask from Photo Sciences, Inc. (Torrance, CA, USA), whose design is shown in Figure S1. The molds were coated with 10:1 volume mixture of precursor:crosslinker of polydimethylsiloxane (PDMS, Slygard 184, Midland, DX, USA), which was de-gassed and cured at 65 °C for 12 h. The PDMS was then carefully pealed from the SU8 mold, resulting in an elastomeric stamp. The stamp was coated with 20 μL of 1 mM ethanolic solution of the thiol-terminated molecular ink mercaptododecanoic acid (MDA, Sigma-Aldrich, St. Louis, MO, USA). After 30 s, the bulk solution was blown off with a stream of air. The stamp was then brought into contact with an Au-coated glass slide for 30 s. The ink molecules absorbed onto the Au surface via thiol-metal bonds, forming a monolayer. The glass slide was rinsed thoroughly with ethanol and then submerged in a 1 mM ethanol solution of thiol-terminated octodecanethiol (ODT, Sigma-Aldrich) background molecules for one hour.

Because self-assembled monolayer (SAM) formation is strongly influenced by diffusion properties of constituent molecules [26], the stamping time is an important parameter. We empirically determined that the optimal stamping time is around 30 s in our system. At higher stamping times, the resulting droplets are larger than the stamp features, which is a result of diffusion along the surface. At shorter times, the LC droplet shapes becomes irregular and non-uniform.

Polarized optical micrographs (POMs) were taken using a custom inverted microscope setup built using optomechanics components with Mitutoyo Plan Apochromat long working distance objectives and a DCC1645C-HQ camera (Thorlabs, Inc., Newton, NJ, USA). A syringe is suspended horizontally next to the stage, with a 90-degree bent needle so that

the tip is normal to the sample surface. The light source above the sample is polarized and an analyzer in front of the camera allows for polarized microscopy. The stage is controlled manually using a micrometer screw while the syringe and microscope components remain stationary.

3. Results and Discussion

3.1. 5CB-SAM Interaction

The static contact angle of the droplets, θ_c, on binary chemically patterned surfaces, can be broken down into three distinct conditions [27]. As is shown in Figure 1, the liquid is designated as α, the gaseous environment is β, the high-wettability domain is γ, and the low-wettability domain is δ. If the droplet is fully contained within the γ-domain (Figure 1a), $\theta_c = \theta_{c,\gamma}$. In the case where the droplet is larger than the γ-domain and its edges are located on the δ-domain (Figure 1b), the contact angle $\theta_c = \theta_{c,\delta}$. Finally, if the droplet is pinned at the interface between the γ- and δ-domains (Figure 1c), the contact angle takes on an intermediate value $\theta_{c,\gamma} < \theta_c < \theta_{c,\delta}$ and is dependent on the volume of the droplet.

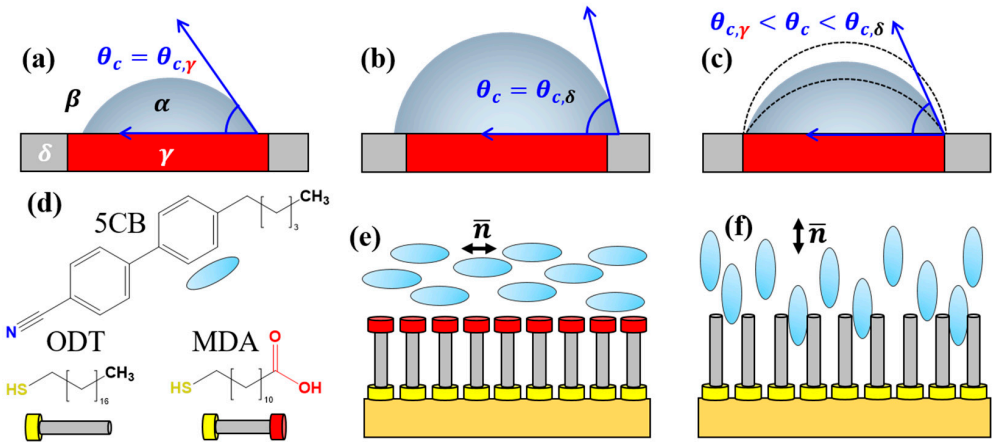

Figure 1. Contact angle of droplets on high and low energy domains. (**a**) Low contact angles are seen on high energy domains. (**b**) When the contact angle is pinned at the domain boundary, the contact angle varies. (**c**) When the droplet edge is in contact only with the low energy domain, a high contact angle is seen. (**d**) Chemical structures and schematic figures of the chemicals used in this work. (**e**) The carboxylic acid groups in MDA form a polar surface that induces planar alignment. (**f**) The long alkyl tails in ODT enforce a non-polar surface that induces homeotropic alignment.

Chemical structures of 5CB, MDA, and ODT are shown in Figure 1d. First, we observed the behavior of 5CB on the hydrophilic MDA. The unconjugated and non-polar dodecyl moiety was used to isolate 5CB from the metallic gold surface. The carboxylic acid terminal group creates an even, polar surface for the 5CB molecules. A schematic of the system is shown in Figure 1e. The 5CB-MDA interaction in air shows high wettability with a contact angle <7°, which is consistent with previous reports of 5CB on carboxylic acid-terminated surfaces in the literature [28]. Between crossed polarizers we observe that the 5CB takes on a planar orientation on the surface. The high wettability suggests that the planar 5CB-MDA interaction is stronger than the homeotropic 5CB–air interaction. Distilled H_2O on MDA exhibited a contact angle of 35°.

We also examined the behavior of 5CB on SAMs of ODT. The purpose of ODT SAMs is to insulate the 5CB from the metallic surface with a non-polar interface. 5CB shows a lower wettability on the ODT surface with a contact angle ~60°. Using polarized optical microscopy, we observe that the orientation is homeotropic. This is likely due to the alkyl chain of the 5CB inserting into the ODT layer [29], as is shown in Figure 1e. Distilled H_2O has low wettability on ODT with a contact angle larger than 100°, verifying that there is a poor interaction of the SAM with polar groups.

3.2. Self-Localization of LC

Droplet arrays were formed on the patterned SAM by taking advantage of the chemical pinning effect [10,11]. The process occurs in four stages (Figure 2a). First, a large (several mm diameter) drop is placed on the patterned surface using a syringe and takes on the static contact angle of the ODT ink, $\theta_{c,\delta}$. When the substrate beings to move, the drop is anchored by the syringe and gets stretched until the back of the drop take on its receding contact angle for the δ-surface $\theta_{r\delta}$. At this point, the back edges of the drop begin to slide across the surface with a constant contact angle $\theta_{r\delta}$ until it reaches a γ-domain. Because $\theta_{r\delta} > \theta_{r\gamma}$, the drop becomes pinned at the back of the domain as it gets further stretched while the rest of the drop continues to slide along the sides of the domain. Near the end of the process, only a narrow fluid bridge remains between the pinned fluid and the moving drop, highlighted in Figure 2b (see Supplementary Materials Video S1). When this breaks, a droplet is left in the wake of the large drop with a static contact angle $\theta_{c,\gamma} < \theta_c < \theta_{c,\delta}$. Droplets that have a contact angle smaller than $\theta_{c,\gamma}$ at the time of formation will contract on the γ-domain, as is shown in the center of the ESEM image in Figure 2c, where the droplets in black are shown sitting on larger dark-grey regions of the MDA ink.

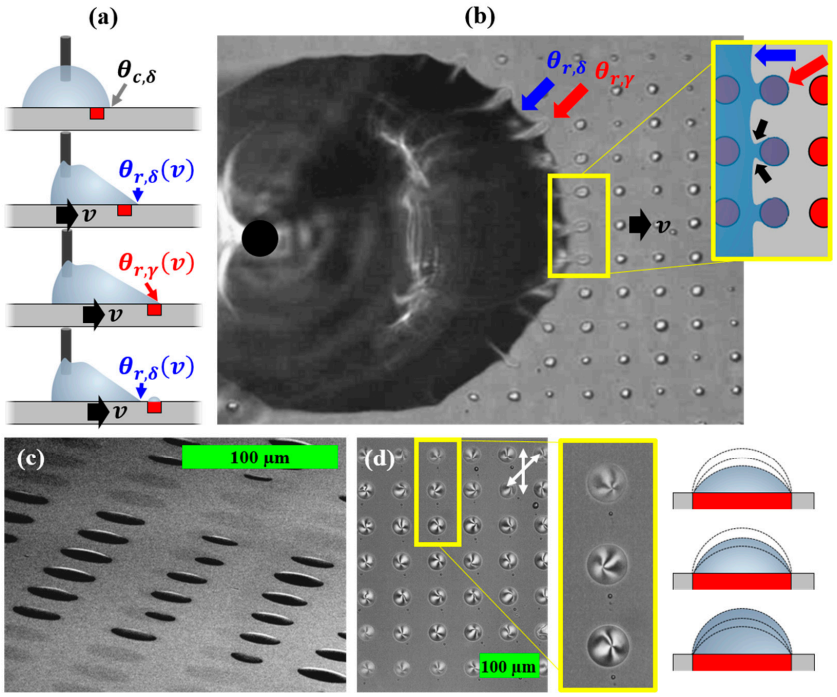

Figure 2. Dragged-drop method used to generate LC arrays. (**a**) A schematic method where the syringe is kept stationary while the chemically-patterned surface is moving to the right, causing droplets to form on the right edge of the large drop. Blue and red arrows show the receding contact angle on the LC-phobic and LC-philic region, respectively. (**b**) An image of the droplet nucleation process taken on a custom microscope. Yellow inset shows droplets pinching off of the larger drop. (**c**) ESEM image of liquid crystal droplets on a chemically patterned surface after individual passes using the dragged-drop method. Droplets are contained on the dark regions on the surface, which indicate the oxygen content of the MDA ink. More images are included in the Supplementary Material Figure S3. (**d**) A POM image of the droplet array after a single pass. White arrows show the orientation of the polarizer and analyzer. The yellow inset highlights the difference in droplet size between the center and the periphery of the dragged-drop, schematically shown on the right.

From our studies, the volume of the pinched off droplets is dependent on three factors: the relevant contact angles, the velocity of the moving drop, and the location of the pinched off droplets to the center of the dragged drop. The larger the discrepancy between the receding contact angle on the δ-surface and the γ-domain, the larger the contact angle of

the droplet. This can be controlled chemically by the inks used or by the speed of the drop, because receding contact angles have varying velocity dependence. In this work, we used a velocity of ~1 µm/s, which was roughly controlled by manually turning a micrometer screw on a translation stage. We noticed that the droplets that formed at the periphery of the drop tended to be thinner than those formed near the center, which is shown in Figure 2d. We theorize that this is due to the curvature of the drop at the periphery, which results in a receding edge that is not perpendicular to the motion. As a result, the fluid bridge is larger and fluid on the γ-domain deforms further before breaking off from the main drop.

The influence of fluid anisotropy on this process is beyond the scope of this work. Although we would expect that the difference in alignment on ODT and MDA, in addition to the LC's elastic response to deformation, could play a role in either suppressing or enhancing droplet self-localization, our understanding of the process does not differentiate between isotropic and anisotropic fluids.

3.3. LC Droplets

3.3.1. Droplets of Nematic LC

The topological confinement of LC droplets on surfaces is sensitive to the anchoring of the constituent molecules at the surface. As a result, observing drop topology using POM is commonly used to determine local surface anchoring conditions [30–34]. Topological constraints of a homeotropically aligned curved air–5CB surface and planar degenerate anchoring at the MDA–5CB surface results in a single +1 boojum defect embedded at the center of the SAM. This leads to a continuous four-brush pattern, shown in Figure 3a–c. In larger droplets with diameters ~30 µm, the location of the defect can be significantly off-center, as is shown in Figure 3a. This is due to surface inhomogeneities at the surface that pin the defect.

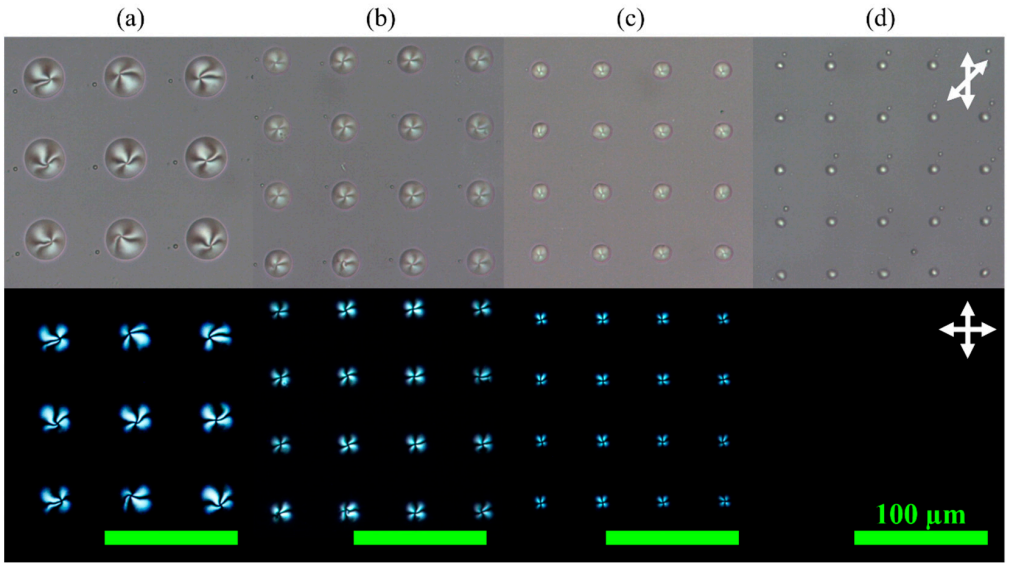

Figure 3. POM of nematic LC droplet arrays. Droplet diameters are (**a**) 30 µm, (**b**) 20 µm, (**c**) 15 µm, and (**d**) 5 µm. The top row is viewed with a 45° angle between the polarizer and analyzer, whereas the bottom row is viewed through crossed polarizers, as indicated by the white arrows in the top right corners.

As the diameter decreases (Figure 3b,c), the homeotropically aligned curved surface generates more internal strain on the LC orientational elasticity and pushes the defects more reliably into the center. As the size decreases further, the mismatch of the surface anchoring conditions breaks the order of the LC, leading to a complete loss of anisotropy, which can be seen in Figure 3d. We expect that the diameter required to achieve homogeneous

droplet structures (~15 µm) is strongly dependent on the contact angle, but our results are consistent with those demonstrated in micro-wells of ~10 µm [35].

3.3.2. Droplets of Cholesteric LC

In the bulk, cholesteric LC takes on a chiral order to minimize its free energy. By confining this LC into µm-sized droplet arrays, we observed the effect this has on the POM texture. The natural pitch of the LC is 1 µm at room temperature. In small droplets of around 10 µm (Figure 4a), the four-brush pattern can be easily seen as the surface alignment dominates the internal elastic energy of the droplet. As the droplets become larger (Figure 4b), the brush pattern becomes distorted as the chiral contribution becomes more pronounced. Finally, in droplets around 30 µm in diameter, the POM shows a highly knotted complex metastable state [36,37] with defect lines pinned at the SAM interface and twisting through one another.

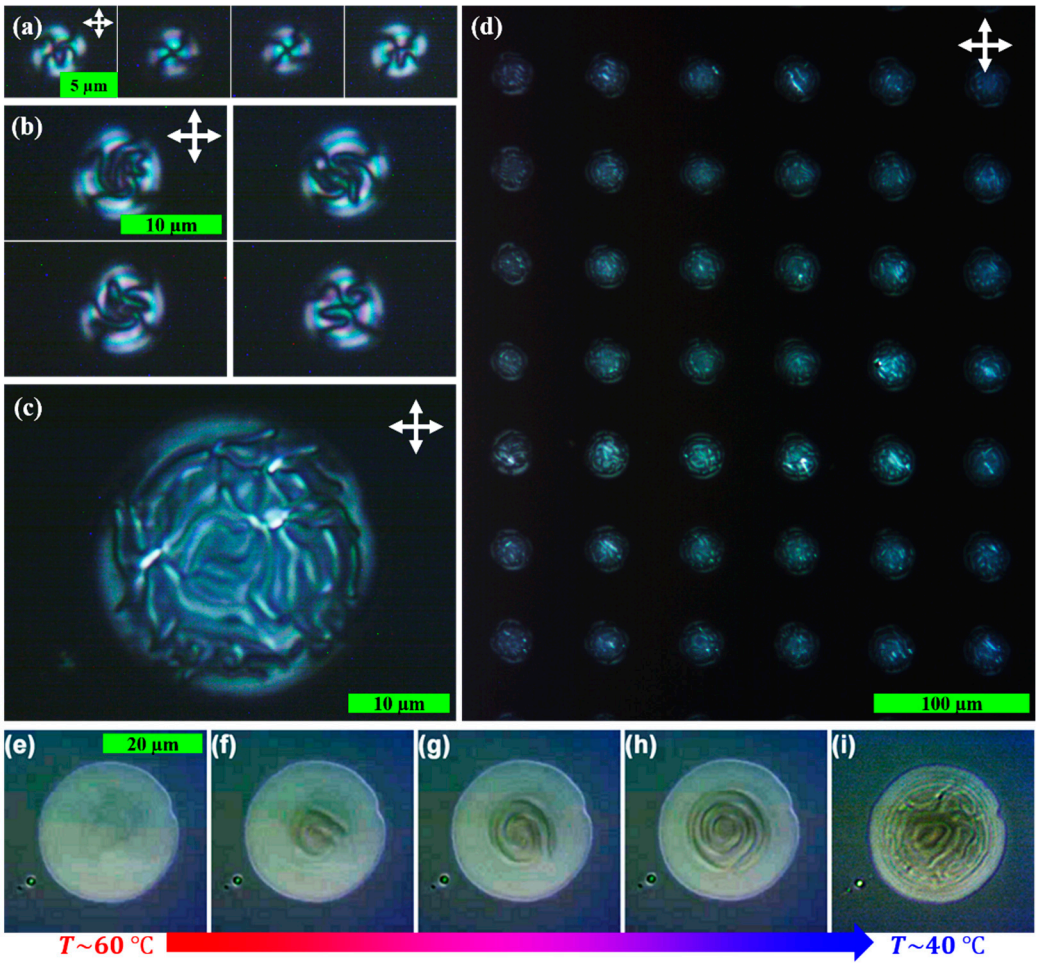

Figure 4. Self-localized cholesteric droplets. Characteristic images of (**a**) 10 µm (**b**) 12.5 µm, and (**c**) 30 µm droplets. (**d**) Array of 30 µm cholesteric droplets. (**e**–**i**) 30 µm droplet of a cholesteric LC with decreasing temperature.

Using temperature to vary the pitch of the LC, we further explored the effect of confinement. With a custom mixture, the pitch increases with temperature. As the 30 µm droplets are heated, the knotted structure generally remains due to strongly pinned defect lines at the SAM surface until the fluid transitions to the isotropic phase (see Supplementary Materials Video S2). However, as the droplet is cooled from the isotropic, the large pitch cholesteric phase appears as a spiral in the center of the droplet (Figure 4f, Supplemental Materials Video S3), with a region of isotropic LC in the regions of smaller thickness. The spiral texture is similar to that of the Frank–Pryce structure observed in spherulites [38] and

spherical droplets [9]. However, in the case of spherical caps, the characteristic defect line from the Frank–Pryce structure is removed by the surface and a simple spiral remains. This is likely due to surface-induced disorder at the SAM interface, which keeps the LC in the isotropic phase, reducing the surface anchoring energy and allowing the chiral structure to resolve without forming additional defects. As the droplet cools further, the spiral grows (Figure 4g,h) until it reaches an abrupt transition where the highly knotted structure again appears (Figure 4i). This final step corresponds to the transition of the LC to the nematic phase at the surface.

4. Conclusions

In this work, we exploited the properties of strong planar and weak homeotropic inks to chemically pattern surfaces to induce self-localization of discrete LC droplets. We presented a phenomenological understanding of this process based on pinning of receding contact angles by two inks that would traditionally be considered LC-philic. The method allowed us to generate a range of LC droplet arrays with great fidelity while varying droplet diameters to explore the effect of geometric confinement on LC topology. Using POM, we observed both the effect of droplet size on liquid crystals and the effect of varying the pitch of a cholesteric LC.

This method can easily be adapted to self-localize LCs with varying properties simultaneously on the surface using multiple syringes. It can enable the roll-to-roll processing of bio/chemo-responsive LC arrays and optical devices.

Supplementary Materials: The following are available online at https://www.mdpi.com/article/10.3390/cryst12010013/s1, Video S1: Dragged Drop.mp4; Video S2: Droplet Heating.mp4; Video S3: Droplet Cooling.mp4; Figure S1: Photomask layout for μ-contact printing (μcp) with circle diameters and periods in the table on the left. The distance between adjacent circles is 30 μm; Figure S2: Microscope images of the elastomeric stamp used for μcp (top) compared to the self-localized LC droplet images (bottom 2 rows). Measured sizes are shown at the bottom of the images. Colored circles are drawn as guides from the elastomeric stamps; Figure S3: ESEM micrographs of LC localized on the μcp surface after individual passes of the LC drop. The SAM pattern is visible as light and dark regions outside of the LC-droplet regions. Light areas correspond to the alkyl chains of ODT while dark regions show the carboxylic acid groups of MDA.

Author Contributions: Conceptualization, J.K. and Q.-H.W.; methodology, J.K.; validation, J.K.; formal analysis, J.K.; investigation, J.K.; resources, Q.-H.W.; data curation, J.K.; writing—original draft preparation, J.K.; writing—review and editing, Q.-H.W.; visualization, J.K.; supervision, Q.-H.W.; project administration, Q.-H.W.; funding acquisition, J.K. and Q.-H.W. All authors have read and agreed to the published version of the manuscript.

Funding: This research was funded by American Chemical Society (ACS PRF 53018-ND7); National Science Foundation (NSF ECCS-0954976); Integrative Graduate Education and Research Traineeship (DGE-0903560).

Acknowledgments: The authors thank LC Chien and Yannian Li for materials, and Julio Avila for his help developing SAM deposition procedures. Acknowledgement is made to the Donors of the American Chemical Society Petroleum.

Conflicts of Interest: The authors declare no conflict of interest.

References

1. Coates, D. Polymer-dispersed Liquid Crystals. *J. Mater. Chem.* **1995**, *5*, 2063. [CrossRef]
2. Baetens, R.; Jelle, B.P.; Gustavsen, A. Properties, requirements and possibilities of smart windows for dynamic daylight and solar energy control in buildings: A state-of-the-art review. *Sol. Energy Mater. Sol. Cells* **2010**, *94*, 87–105. [CrossRef]
3. Sage, I. Thermochromic Liquid Crystals in Devices. In *Liquid Crystals Applications and Uses*; World Scientific Publishing Co. Pte. Ltd.: Singapore, 1992; pp. 301–339.
4. Gardiner, D.J.; Hsiao, W.K.; Morris, S.M.; Hands, P.J.W.; Wilkinson, T.D.; Hutchings, I.M.; Coles, H.J. Printed photonic arrays from self-organized chiral nematic liquid crystals. *Soft Matter* **2012**, *8*, 9977–9980. [CrossRef]

5. Woltman, S.J.; Jay, G.D.; Crawford, G.P. Liquid-crystal materials find a new order in biomedical applications. *Nat. Mater.* **2007**, *6*, 929–938. [CrossRef] [PubMed]
6. Carlton, R.J.; Hunter, J.T.; Miller, D.S.; Abbasi, R.; Mushenheim, P.C.; Tan, L.N.; Abbott, N.L. Chemical and biological sensing using liquid crystals. *Liq. Cryst. Rev.* **2013**, *1*, 29–51. [CrossRef]
7. Sengupta, A.; Herminghaus, S.; Bahr, C. Liquid crystal microfluidics: Surface, elastic and viscous interactions at microscales. *Liq. Cryst. Rev.* **2014**, *2*, 73–110. [CrossRef]
8. Aliño, V.J.; Sim, P.H.; Choy, W.T.; Fraser, A.; Yang, K.L. Detecting proteins in microfluidic channels decorated with liquid crystal sensing dots. *Langmuir* **2012**, *28*, 17571–17577. [CrossRef] [PubMed]
9. Lopez-Leon, T.; Fernandez-Nieves, A. Drops and shells of liquid crystal. *Colloid Polym. Sci.* **2011**, *289*, 345–359. [CrossRef]
10. Nakajima, A.; Nakagawa, Y.; Furuta, T.; Sakai, M.; Isobe, T.; Matsushita, S. Sliding of water droplets on smooth hydrophobic silane coatings with regular triangle hydrophilic regions. *Langmuir* **2013**, *29*, 9269–9275. [CrossRef] [PubMed]
11. Furuta, T.; Sakai, M.; Isobe, T.; Matsushita, S.; Nakajima, A. Sliding of water droplets on hydrophobic surfaces with various hydrophilic region sizes. *Langmuir* **2011**, *27*, 7307–7313. [CrossRef]
12. Jackman, R.J.; Duffy, D.C.; Ostuni, E.; Willmore, N.D.; Whitesides, G.M. Fabricating large arrays of microwells with arbitrary dimensions and filling them using discontinuous dewetting. *Anal. Chem.* **1998**, *70*, 2280–2287. [CrossRef]
13. Feng, W.; Li, L.; Du, X.; Welle, A.; Levkin, P.A. Single-Step Fabrication of High-Density Microdroplet Arrays of Low-Surface-Tension Liquids. *Adv. Mater.* **2016**, *28*, 3202–3208. [CrossRef]
14. Biebuyck, H.A.; Whitesides, G.M. Self-Organization of Organic Liquids on Patterned Self-Assembled Monolayers of Alkanethiolates on Gold. *Langmuir* **1994**, *10*, 2790–2793. [CrossRef]
15. Ueda, E.; Geyer, F.L.; Nedashkivska, V.; Levkin, P.A. DropletMicroarray: Facile formation of arrays of microdroplets and hydrogel micropads for cell screening applications. *Lab Chip* **2012**, *12*, 5218–5224. [CrossRef]
16. Cao, M.; Jiang, L. Superwettability integration: Concepts, design and applications. *Surf. Innov.* **2016**, *4*, 180–194. [CrossRef]
17. Feng, W.; Ueda, E.; Levkin, P.A. Droplet Microarrays: From Surface Patterning to High-Throughput Applications. *Adv. Mater.* **2018**, *30*, 1706111. [CrossRef] [PubMed]
18. Kim, E.; Whitesides, G.M.; Lee, L.K.; Smith, S.P.; Prentiss, M. Fabrication of Arrays of Channel Waveguides by Self-Assembly Using Patterned Organic Monolayers as Templates. *Adv. Mater.* **1996**, *8*, 139–142. [CrossRef]
19. Kobaku, S.P.R.; Kwon, G.; Kota, A.K.; Karunakaran, R.G.; Wong, P.; Lee, D.H.; Tuteja, A. Wettability engendered templated self-assembly (WETS) for fabricating multiphasic particles. *ACS Appl. Mater. Interfaces* **2015**, *7*, 4075–4080. [CrossRef] [PubMed]
20. Lawrence, C.R.; Parker, A.R. Water capture by a desert beetle. *Nature* **2001**, *414*, 33–34.
21. Hamilton, W.J.I.; Seely, M.K. Fog basking by the Namib Desert beetle, Onymacris unguicularis. *Nature* **1976**, *262*, 284–285. [CrossRef]
22. Zhang, L.; Wu, J.; Hedhili, M.N.; Yang, X.; Wang, P. Inkjet printing for direct micropatterning of a superhydrophobic surface: Toward biomimetic fog harvesting surfaces. *J. Mater. Chem. A* **2015**, *3*, 2844–2852. [CrossRef]
23. Lee, M.; Yang, K.; Hwang, Y.H.; Byun, Y.; Lee, D.Y.; Cho, S.-W.; Lee, H. Spheroform: Therapeutic Spheroid-Forming Nanotextured Surfaces Inspired by Desert Beetle Physosterna cribripes. *Adv. Healthc. Mater.* **2015**, *4*, 511–515. [CrossRef]
24. Bao, P.; Paterson, D.A.; Peyman, S.A.; Jones, J.C.; Sandoe, J.A.T.; Bushby, R.J.; Evans, S.D.; Gleeson, H.F. Textures of nematic liquid crystal cylindric-section droplets confined by chemically patterned surfaces. *Crystals* **2021**, *11*, 65. [CrossRef]
25. Wilbur, J.L.; Kumar, A.; Biebuyck, H.A.; Kim, E.; Whitesides, G.M. Microcontact printing of self-assembled monolayers: Applications in microfabrication. *Nanotechnology* **1996**, *7*, 452–457. [CrossRef]
26. Delamarche, E.; Schmid, H.; Bietsch, A.; Larsen, N.B.; Rothuizen, H.; Michel, B.; Biebuyck, H. Transport Mechanisms of Alkanethiols during Microcontact Printing on Gold. *J. Phys. Chem. B* **1998**, *102*, 3324–3334. [CrossRef]
27. Lenz, P.; Lipowsky, R. Morphological Transitions of Wetting Layers on Structured Surfaces. *Phys. Rev. Lett.* **1998**, *80*, 1920–1923. [CrossRef]
28. Park, M.-K.; Jang, C.-H. Liquid Crystal-based Imaging of Biomolecular Interactions at Roller Printed Protein Surfaces. *Bull. Korean Chem. Soc.* **2010**, *31*, 1223–1227. [CrossRef]
29. Popov, P.; Lacks, D.J.; Jákli, A.; Mann, E.K. Insertion of liquid crystal molecules into hydrocarbon monolayers. *J. Chem. Phys.* **2014**, *141*, 054901. [CrossRef]
30. Gupta, V.K.; Abbott, N.L. Using Droplets of Nematic Liquid Crystal to Probe the Microscopic and Mesoscopic Structure of Organic Surfaces. *Langmuir* **1999**, *15*, 7213–7223. [CrossRef]
31. Shah, R.R.; Heinrichs, D.M.; Abbott, N.L. Meso-scale imaging of patterned surfaces by decoration with liquid crystals. *Colloids Surfaces A Physicochem. Eng. Asp.* **2000**, *174*, 197–208. [CrossRef]
32. Mori, N.; Morimoto, M.; Nakamura, K. Hydroxypropylcellulose Films as Alignment Layers for Liquid Crystals. *Macromolecules* **1999**, *32*, 1488–1492. [CrossRef]
33. Yamaguchi, R.; Sato, S. Determination of nematic liquid crystal (NLC) orientation by observing NLC droplets on alignment surfaces. *Jpn. J. Appl. Phys. Part Lett.* **1996**, *35*, L117. [CrossRef]
34. Shen, T.Z.; Hong, S.H.; Lee, J.H.; Kang, S.G.; Lee, B.; Whang, D.; Song, J.K. Selectivity of Threefold Symmetry in Epitaxial Alignment of Liquid Crystal Molecules on Macroscale Single-Crystal Graphene. *Adv. Mater.* **2018**, *30*, 1802441. [CrossRef]
35. Sakanoue, H.; Yamashita, S.; Murakami, T.; Suzuki, H.; Katayama, K. Controlled formation of topological defects of liquid crystals in micro-wells. *Liq. Cryst.* **2021**, *2021*, 1–9. [CrossRef]

36. Seč, D.; Copar, S.; Zumer, S. Topological zoo of free-standing knots in confined chiral nematic fluids. *Nat. Commun.* **2014**, *5*, 3057. [CrossRef]
37. Orlova, T.; Aßhoff, S.J.; Yamaguchi, T.; Katsonis, N.; Brasselet, E. Creation and manipulation of topological states in chiral nematic microspheres. *Nat. Commun.* **2015**, *6*, 7603. [CrossRef]
38. Bouligand, Y.; Livolant, F. The organization of cholesteric spherulites. *J. Phys.* **1984**, *45*, 1899–1923. [CrossRef]